

Opposed-Flow Flame Spread Over Polymeric Materials: Influence of Phase Change

GUANYU ZHENG, INDREK S. WICHMAN,* and ANDRÉ BÉNARD

Department of Mechanical Engineering, Michigan State University, East Lansing, MI 48824, USA

A numerical model for flame spread over polymeric surfaces is constructed. The dependence of the flame spread rate on phase change and thermal properties is investigated by varying three non-dimensional parameters, St , \bar{k}_l , and \bar{C}_{pl} . Quantitative comparisons indicate that the numerical model provides excellent agreement to an analytical formula in the cases of variable latent heat of the phase change, variable liquid thermal capacity, and variable thermal conductivity. However, the deRis formula yields a constant spread rate higher than the numerical result and is independent of phase change. Qualitatively, with the increase of St , or with the decrease of \bar{k}_l or \bar{C}_{pl} , the flame spread rate increases. In addition, \bar{k}_l is the strongest determinant of the influence of the thickness of the liquid region. The mechanisms of flame spread at the steady state are interpreted by applying an energy balance principle for the control volume upstream of the flame leading edge. It is found that a ratio between the total heat applied to the condensed material upstream of the flame leading edge and the spread rate reveals the physical mechanisms that control the preheating of the condensed material to the ignition temperature. The dependence of flame structure on St , \bar{k}_l , and \bar{C}_{pl} is studied. It is found that with the increase of St or \bar{k}_l , or with the decrease of \bar{C}_{pl} , the size of the flame increases. These results indicate that flame size dependence follows the magnitude of the spread rate when the properties of the condensed material are variable. © 2001 by The Combustion Institute

NOMENCLATURE

A_c	pre-exponential factor of pyrolysis reaction in condensed material, s^{-1}	ℓ_{gy}	transverse length of gas phase in computational domain, m
A_g	pre-exponential factor of combustion reaction in gas phase, $m^3/(kg/s)$	Le	Lewis number, α_g/D
C_P	specific heat, $J/(kg/K)$	\hat{l}	unit vector normal to the boundary of the condensed material, (<i>non-dimensional</i>)
\bar{C}_{pl}	nondimensional liquid thermal capacity, C_{pl}/C_{ps}	L_s	latent heat of melting, J/kg
D	diffusion coefficient, m^2/s	\dot{m}	mass flow rate through gas-condensed interface, $kg/(m^2/s)$
E_c	activation energy of pyrolysis reaction in solid phase, J/mol	\bar{m}_{liquid}	mass of liquid in the condensed material, kg
E_g	activation energy of combustion reaction in gas phase, J/mol	M	molecular weight of species, g/mol
h	reference length for nondimensionalization, m	n^*	unit vector normal to moving solid-liquid interface in condensed material, (<i>non-dimensional</i>)
h_c	enthalpy of condensed material, J/kg	q_g	heat of combustion reaction in gas phase, J/kg
k	thermal conductivity, $W/(m \cdot K)$	\dot{q}_{ig}	radiant heat flux for ignition, $J/(m^2/s)$
\bar{k}_l	nondimension liquid conductivity, k_l/k_s	\bar{q}_{ig}	average net heat flux into the condensed material before ignition, W
K_e	permeability factor of pyrolysis products, (<i>non-dimensional</i>)	q_c	heat of pyrolysis reaction in condensed material, J/kg
ℓ_x	streamwise length of computational domain, m	Q_{lat}	latent enthalpy increase (associated with phase change) of the condensed material at ignition, (<i>non-dimensional</i>)
ℓ_{sy}	transverse length of condensed material in computational domain (the thickness of the polymer), m	Q_{sen}	sensible enthalpy increase (associated with temperature increase) of the

*Corresponding author. E-mail: wichman@egr.msu.edu

	condensed material at ignition, (<i>non-dimensional</i>)
R	universal gas constant, 8314 J/(mol/K)
St	Stefan number, $C_{Ps}(T_m - T_\infty)/L_s$
t	time, s
T	temperature, K
T_m	melting temperature of condensed material, K
u_s	flame spread rate, m/s
u_∞	velocity of opposed flow, m/s
v_{n^*}	velocity of moving solid-liquid interface, m/s
w_g	mass rate of fuel consumption in combustion reaction of gas phase, kg/(m ³ /s)
w_s	mass rate of production of monomer in pyrolysis reaction of condensed material, kg/(m ³ /s)
x	streamwise distance downstream from origin, m
y	transverse distance normal to the interface between the gas phase and the condensed material, m
Y	mass fraction of species in gas phase, (<i>non-dimensional</i>)

Greek

α	thermal diffusivity $\alpha = k/\rho C_p$, m ² /s
ϵ	surface emittance, (<i>non-dimensional</i>)
μ	stoichiometric coefficient, (<i>non-dimensional</i>)
ρ	density, kg/m ³
σ	Stefan-Boltzmann constant, (<i>non-dimensional</i>)
τ	reference time for nondimensionalization, s
τ_{ig}	ignition delay time, s
Σ	solid-liquid interface in condensed material
Ω	coefficient for nondimensionalization $\Omega = \alpha_s/\alpha_g$, (<i>non-dimensional</i>)

Subscript

c	condensed material
f	fuel in gas phase
g	gas phase
i	interface between gas phase and condensed phase
l	liquid in condensed material
o	oxidizer in gas phase

s	solid in condensed material
∞	initial condition
Σ	interface between liquid phase and solid phase

INTRODUCTION

Transient flame growth over polymeric materials is important in fire safety, and has theoretical and pedagogical importance in basic combustion science research and education. The latter stems from a large number of complicated phenomena, their mutual influences, and the challenge of describing them in an orderly, logical manner.

When a polymeric material is subjected at a portion of its exposed surface to a high heat flux, it can be ignited. The ignition of flame may lead to subsequent flame spread. Because surface ignition at a point is associated with induced inflow of air (oxidizer), we will be concerned in the model with flame spread against an induced or forced opposing flow of oxidizer.

An extensive research literature exists for this class of flame spread problem, see the reviews of [1–3]. Most of the literature addresses solid fuels. The review of Ref. [4] addresses flame spread over liquid fuels, which possess additional complications such as surface driven flow, enhanced buoyancy and liquid vaporization, etc. These complications are potentially important when the liquid phase melt layer actually precedes the flame leading edge. Heat transfer ahead of the flame by liquid phase convection may be important under same conditions. In addition, recirculating cells may develop in the gas and pulsating spread may be possible. Then, a significant overlap may occur between flame over initially solid fuels (which liquefy) and flame spread over liquid fuels.

Many formulations of the theoretical opposed-flow flame spread problem have appeared in the research literature. The study of deRis [5] stands out as the first systematic examination including simplified gas-phase chemistry, solid decomposition, multi-dimensional transport, and convective/buoyant flow. Many other models were subsequently examined (see [3]) but only one studied flame spread from a global energy balance perspective, thus,

adding insight into the flame spread process [6]. The importance of the global balance principle arises from the ease with which it can be used to derive flame spread formulas under conditions more general than those for which it was derived. The global balance principle is easy to apply because of the neglect of streamwise conduction. Instead of solving complicated elliptic boundary value problems, relatively simple parabolic conservation equations can be formulated, which balance streamwise convection and cross-stream conduction.

By utilizing the global balance principle a flame spread formula for charring materials was derived ([8], see the discussion of [8] in [3]). This formula is perhaps more suitable for a solid that liquefies upon heating because liquefaction is a simpler process than solid pyrolysis and degradation, and usually occurs along or near a specific isotherm. However, it is well known that solid degradation and pyrolysis does not occur at a specific isotherm. We shall demonstrate that our model for flame spread over a melted polymer agrees, under many conditions, extremely well with predictions of the flame spread formula where considerations of dripping and running are not included in either model or theory. The flame spread formula therefore can be interpreted physically in terms of local physics near the point of flame attachment. Recent work on transient solid-phase ignition and flame spread has been undertaken by Kashiwagi, Baum, and colleagues on microgravity flame initiation on cellulosic materials [9]. A detailed model of the gas flow and its thermal expansion during ignition and spread was developed and then solved numerically.

It is known that many complicated, simultaneous processes occur in the solid with gas-phase combustion above it. These include detailed degradation chemistry, anisotropic conduction, phase change, bubble formation and transport, charring of the surface, pitting, and condensed-matter expulsion at the surface. Because of these and other complexities, the condensed phase has been studied considerably less than the gas phase [10]. Studies of flame spread over melting polymers have rarely been reported except for some experimental observations [10].

The purpose of this article is to examine a

flame spread model whose solid (or condensed) phase contains some solid phase complexities not described previously in flame spread research [1–14]. The gas will be described by a standard Oseen-flow model. Finite-rate gas chemistry is retained. In the condensed material, we retain phase change (solid \rightarrow liquid in-depth; liquid \rightarrow gas at surface). Upon phase change, thermophysical properties (conductivity, and specific heat) may change.

Our numerical model will be transient, enabling computation from incipient heating to flame ignition to eventual steady spread. Melting and phase change alter ignition. Comparisons are made with predictions of theory in the steady state. The eventual goal of our research is to include bubble formation in the liquid melt layer. The study of flame spread with phase change of the fuel from solid to pure liquid is a first step.

NUMERICAL MODEL

Problem Formulation

A schematic formulation of the problem is provided in Fig. 1. Some simplifications are made to reduce the complexity of the governing equations that describe unsteady flame initiation and spread over polymeric materials. First, the Oseen approximation of uniform velocity profile is used, thereby: (1) eliminating the momentum equations from the solution; (2) uncoupling the velocity field from the thermal and chemical fields; (3) reducing the N-S equations to the constant pressure condition if the opposed flow Mach number is negligibly small. Flame spread is considered to occur in the horizontal plane, thereby eliminating required consideration in the vertical configuration of melt flow from the melting surface. The authors are unaware of any theoretical or numerical work on this subject outside of preliminary work in a highly idealized configuration [15, 16]. Second, radiation absorption by the flame and radiant emission from the flame are ignored, as are surface and in-depth radiant absorption by the condensed material. Third, the thermal properties and kinetic data (pre-exponential factor and activation energy) are assumed con-

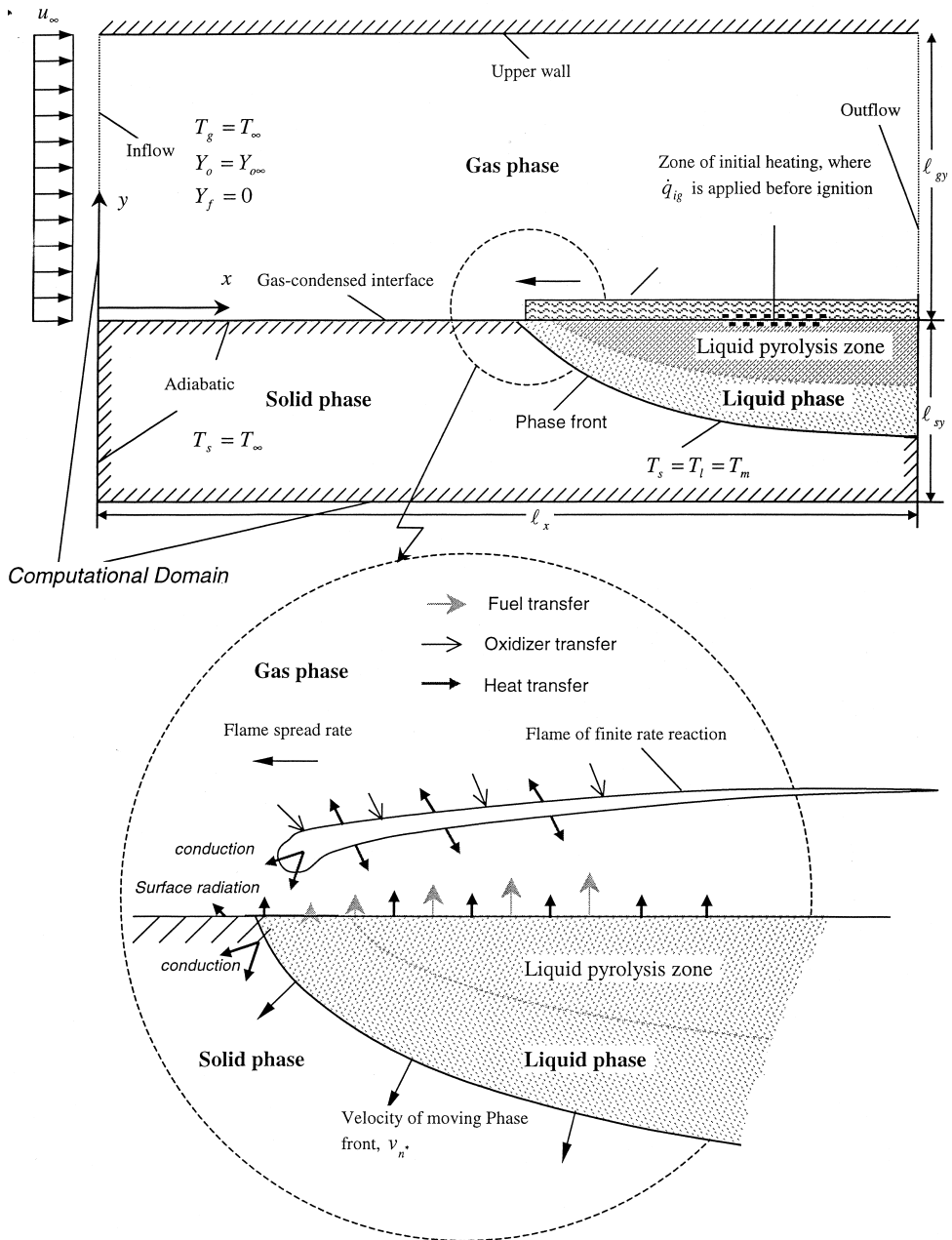


Fig. 1. Schematic description of diffusion flame spread over polymers in an opposed-flow of oxidizer.

stant. Fourth, the regression or deformation of the gas-condensed interface and Marangoni flow of polymer melt near the interface are assumed negligible. The other assumptions that are relevant to the specific equations will be introduced hereafter. All restrictions are removable in principle, but when initial studies are conducted in a simple manner, the compli-

cations that are later introduced are more clearly understood. Some of our restrictions (negligible interface regression, no surface Marangoni flow) have not been extensively studied in the context of flame spread. The governing equations include those for the transient reactive gas phase, the transient reactive condensed phase, the non-reactive gas-condensed inter-

face, and boundary conditions. The origin of coordinates is fixed at the interface, therefore the subscript “ $y > 0$ ” denotes the gas phase, while the subscript “ $y < 0$ ” denotes the condensed phase.

The transport mechanisms in the gas phase include diffusion, streamwise convection, and chemical reaction. The species and energy conservation equations are given by

$$\rho_g \left[\frac{\partial Y_i}{\partial t} + u_\infty \frac{\partial Y_i}{\partial x} \right] = \rho_g D \nabla^2 Y_i + \mu_i w_g, \quad (1)$$

$$i = f, o, \quad y > 0,$$

$$\rho_g C_{Pg} \left[\frac{\partial T}{\partial t} + u_\infty \frac{\partial T}{\partial x} \right] = k_g \nabla^2 T + q_g w_g, \quad (2)$$

$$y > 0.$$

It is assumed that the combustion reaction $F + \nu_o O \rightarrow P$ is an overall single-step, irreversible second-order Arrhenius reaction, with reaction rate $w_g = -\rho_g^2 Y_o Y_f A_g e^{-E_g/RT}$ and stoichiometric ratio $\mu_i = M_i \nu_i / M_f \nu_f$, $i = f, o$. The heat transfer mechanisms in the condensed material include thermal diffusion, phase change, and pyrolysis reaction. The energy conservation equation in enthalpy form is

$$\rho_c \frac{\partial h_c}{\partial t} = k_c \nabla^2 T + q_c w_c, \quad y < 0, \quad (3-a)$$

where subscript “ c ” denotes the condensed material in general, and will be denoted by “ l ” or “ s ” in individual liquid and solid phases, respectively. An overall single-step first-order Arrhenius reaction of *polymer* \rightarrow *monomer* is assumed for the pyrolysis process, with reaction rate $w_c = -\rho_c A_c \exp(-E_c/RT)$. The condensed-phase density ρ_c may take the form of ρ_l or ρ_s in the condensed material. The kinetic data for E_c and A_c are constants for both solid and liquid phases. The enthalpy-temperature relationship in Fig. 2 is provided along with Eq. 3-a, thereby reducing two unknowns (enthalpy and temperature) to one. In Fig. 2, phase change is assumed to take place at a fixed melting temperature T_m ,¹ and the thermal properties ρ , C_p ,

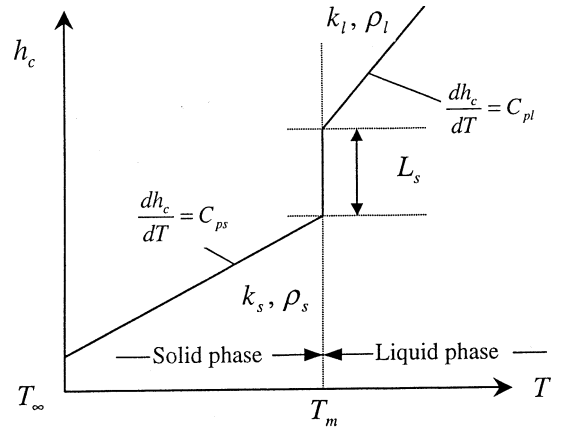


Fig. 2. The enthalpy-temperature relationship used in the model.

and k in the solid and liquid are assumed constant in each phase, but not necessarily the same. This implies the existence of discontinuous thermal properties across the solid-liquid interface. The energy conservation equation of the condensed material in temperature form includes three domains of interest, viz., the solid phase, the liquid phase and the moving phase front,

$$\begin{cases} \rho_s C_{Ps} \frac{\partial T}{\partial t} = k_s \nabla^2 T - q_c w_c, & \text{solid} \\ \rho_l C_{Pl} \frac{\partial T}{\partial t} = k_l \nabla^2 T - q_c w_c, & \text{liquid} \end{cases}, \quad y < 0 \quad (3-b)$$

$$\begin{cases} -\left(k \frac{\partial T}{\partial n^*}\right)_s + \rho L_s v_{n^*} = -\left(k \frac{\partial T}{\partial n^*}\right)_l, \\ T_\Sigma = T_m \end{cases}, \quad (3-c)$$

$$\text{phase front}, \quad y < 0$$

Eqs. 3-b i, ii are the energy conservation equations for the solid and liquid, respectively. Eq. 3-c is the Stefan condition in vector form, where n^* denotes the unit vector normal to the moving solid-liquid phase front Σ , and v_{n^*} denotes the phase front velocity.

At the gas/condensed phase interface, the mass transfer mechanism is pure diffusion of the net normal flow comprising pyrolysis products. The heat transfer mechanisms include conduction in the gas, conduction in the solid, surface radiation to the environment, and transient ignition heat flux \dot{q}_{ig} , which is applied

¹The melting point of the polymer is different from the ‘glassy point’ temperature that frequently appears in the literature, and normally has a larger value.

before ignition and removed thereafter. The species and energy transport processes are assumed to be always equilibrated, whereby

$$\begin{cases} -\rho_g D \frac{\partial Y_f}{\partial y} \Big|_{0+} = (1 - Y_f|_{0+}) \dot{m}, \\ -\rho_g D \frac{\partial Y_o}{\partial y} \Big|_{0+} = (0 - Y_o|_{0+}) \dot{m}, \\ -k_s \frac{\partial T}{\partial y} \Big|_{0-} = -k_g \frac{\partial T}{\partial y} \Big|_{0+} + \epsilon \sigma (T^4 - T_\infty^4) - \dot{q}_{ig}. \end{cases} \quad (4-a)$$

In Eqs. 4-a i, ii, iii, the mass flow rate \dot{m} arises from the pyrolysis products. The virtual mass flow rate of condensed phase pyrolysis products can be written in integral form as $\int_{-\ell_{sy}}^0 w_c dy$. A permeability factor K_e with range between zero and unity is used to adjust the magnitude of this mass flow rate. Hence,

$$\dot{m} = K_e \int_{-\ell_{sy}}^0 w_c dy. \quad (4-b)$$

This equation implies that the transport of gas through the liquid is a steady process, because no storage effect or time derivative appears. The heat transfer described by Eq. 3-b, however, is unsteady. Usually, when diffusion is the transport mechanism, mass transfer through liquids is slower than heat transfer. Our model acknowledges this limitation, but is applicable (valid) in the limit that the liquid layer contains a uniform distribution of “gas” molecules that finally escape from the surface. There is a uniform and continual migration of monomer molecules toward the surface. Of course, this is an idealization that is, in principle, removable when the solid phase degradation is better understood. The gas in this model may be interpreted as molecules of monomers, which form in the liquid layers of thickness l_{sy} that escape from the surface. In other words, Eq. 4-b states that \dot{m} is proportional to the integral of w_c over the solid thickness, but the mass, in fact, escapes from the surface cell after the reaction *polymer* \rightarrow *monomer* has taken place. In the gas, an isothermal inflow boundary condition and an adiabatic outflow boundary condition are applied at $x = 0, 0 < y < \ell_{gy}$, and at $x = \ell_x, 0 < y < \ell_{gy}$, respectively, where ℓ denotes the linear dimension of the computational domain. A closed adiabatic boundary condition is applied

at the upper wall $y = \ell_{gy}, 0 < x < \ell_x$, as indicated below. Other boundary conditions include

$$\begin{cases} x = 0, 0 < y < \ell_{gy} \\ \left. \begin{aligned} T &= T_\infty \\ Y_o &= Y_{0\infty}; x = \ell_x, 0 < y < \ell_{gy} \\ Y_f &= 0 \end{aligned} \right\} \\ \left. \begin{aligned} \frac{\partial T}{\partial x} &= 0 \\ \frac{\partial Y_i}{\partial x} &= 0, i = o, f \end{aligned} \right\} \end{cases}$$

The adiabatic condition is written as:

$$y = \ell_{gy}, 0 < x < \ell_x \left\{ \begin{aligned} \frac{\partial T}{\partial y} &= 0, \\ \frac{\partial Y_i}{\partial y} &= 0, i = o, f. \end{aligned} \right. \quad (5-a)$$

In the condensed phase, the remaining three boundary conditions are all adiabatic.

$$\begin{aligned} x = 0, -\ell_{sy} < y < 0 \text{ or } x = \ell_x, -\ell_{sy} < y < 0 \text{ or} \\ y = -\ell_{sy}, 0 < x < \ell_x \frac{\partial T}{\partial \hat{t}} = 0. \end{aligned} \quad (5-b)$$

The initial condition is

$$T = T_\infty, Y_f = 0 \text{ and } Y_o = Y_{0\infty}, \quad (6)$$

where Y_o is the initial or inflow oxidizer mass fraction in the gas.

The conservation Eqs. 1–3, the gas-condensed interface condition 4, boundary conditions 5 and initial condition 6 together form a well posed unsteady nonlinear boundary value problem.

Nondimensionalization

The governing equations shall be nondimensionalized to analyze physical mechanisms that may subsequently influence flame development. It is difficult to derive appropriate reference variables for dimensional analysis. If phase change is negligible, the dominant mechanism of heat transfer in the solid for flame spread over thermally thick fuel is solid heat conduction [1]. However, for polymers with a low melting point and low viscosity, it was observed

[10] that phase change and melt flow may influence flame spread. Gas phase conduction is dominant in thermally thin flame spread and becomes weaker as the fuel thickens [1]. Whatever the relative importance of a certain heat transfer mechanism is, the interactions between the gas and the condensed phases always determines the nature of flame growth and spread. Based on this idea, the nondimensionalization is carried out as follows: the reference length $h = \alpha_s/u_\infty$ is obtained by multiplying the characteristic thermal length in the gas (α_g/u_∞) by a factor $\Omega = \alpha_s/\alpha_g$; the reference time is $\tau = h/u_\infty$; the reference temperature is L_s/C_{ps} ; the reference oxidizer concentration is $Y_{o\infty}$; the reference fuel concentration is $Y_{o\infty}/\mu_o$.

In summary, the coordinates x and y are nondimensionalized as $\bar{x} = x/h$ and $\bar{y} = y/h$; time t is nondimensionalized as $\bar{t} = t/\tau$; temperature T is nondimensionalized as $\bar{T} = C_{ps}(T - T_\infty)/L_s$; the fuel concentration is nondimensionalized as $\bar{Y}_f = Y_f\mu_o/Y_{o\infty}$; and the oxidizer concentration is nondimensionalized as $\bar{Y}_o = Y_o/Y_{o\infty}$. The dimensionless equations, interface conditions, boundary, and initial conditions are,

Gas phase;

$$\frac{\partial \bar{Y}_i}{\partial \bar{t}} + \frac{\partial \bar{Y}_i}{\partial \bar{x}} = \frac{1}{\Omega Le} \left(\frac{\partial^2 \bar{Y}_i}{\partial \bar{x}^2} + \frac{\partial^2 \bar{Y}_i}{\partial \bar{y}^2} \right) + \bar{w}_g, \quad i = f, o, \quad i = f, o \quad (7)$$

$$\frac{\partial \bar{T}}{\partial \bar{t}} + \frac{\partial \bar{T}}{\partial \bar{x}} = \frac{1}{\Omega} \left(\frac{\partial^2 \bar{T}}{\partial \bar{x}^2} + \frac{\partial^2 \bar{T}}{\partial \bar{y}^2} \right) + \bar{q}_g \bar{w}_g, \quad i = f, o \quad (8)$$

Condensed phase (temperature form);

$$\begin{cases} \frac{\partial \bar{T}_s}{\partial \bar{t}} = \frac{\partial^2 \bar{T}_s}{\partial \bar{x}^2} + \frac{\partial^2 \bar{T}_s}{\partial \bar{y}^2} - \bar{q}_c \bar{w}_c, & \text{in the solid} \\ \bar{\rho}_l \bar{C}_{pl} \frac{\partial \bar{T}_l}{\partial \bar{t}} = \bar{k}_l \left(\frac{\partial^2 \bar{T}_l}{\partial \bar{x}^2} + \frac{\partial^2 \bar{T}_l}{\partial \bar{y}^2} \right) - \bar{q}_c \bar{w}_c, & \text{in the liquid} \end{cases}, \quad \bar{y} < 0 \quad (9-a)$$

$$\begin{cases} -\frac{\partial \bar{T}_s}{\partial \bar{n}^*} + \bar{v}_{n^*} = -\bar{k}_l \frac{\partial \bar{T}_l}{\partial \bar{n}^*}, & \text{phase front, } \bar{y} < 0 \\ \bar{T}_\Sigma = St \end{cases} \quad (9-b)$$

Gas/condensed phase interface;

$$\begin{cases} -\frac{1}{\Omega Le} \frac{\partial \bar{Y}_f}{\partial \bar{y}} \Big|_{0+} = \bar{m} \left(\frac{\mu_o}{Y_{o\infty}} - \bar{Y}_f \Big|_{0+} \right) \\ -\frac{1}{\Omega Le} \frac{\partial \bar{Y}_o}{\partial \bar{y}} \Big|_{0+} = \bar{m} (0 - \bar{Y}_o|_{0+}), \quad y = 0 \\ \frac{\partial \bar{T}}{\partial \bar{y}} \Big|_{0-} = -\frac{k_g}{k_s} \frac{\partial \bar{T}}{\partial \bar{y}} \Big|_{0+} + \bar{\omega} [(\bar{T} + \bar{T}_\infty)^4 - \bar{T}_\infty^4] - \bar{q}_{ig} \end{cases} \quad (10)$$

Boundary conditions;

$$\begin{aligned} \bar{x} = 0, 0 < \bar{y} < \bar{\ell}_{gy} \\ \begin{cases} \bar{T} = 0 \\ \bar{Y}_f = 0; \bar{x} = \bar{\ell}_x, 0 < \bar{y} < \bar{\ell}_{gy} \\ \bar{Y}_o = 0 \end{cases} \begin{cases} \frac{\partial \bar{T}}{\partial \bar{x}} = 0 \\ \frac{\partial \bar{Y}_i}{\partial \bar{x}} = 0, i = o, f \end{cases}; \\ \bar{y} = \bar{\ell}_{gy}, 0 < \bar{x} < \bar{\ell}_x \begin{cases} \frac{\partial \bar{T}}{\partial \bar{y}} = 0 \\ \frac{\partial \bar{Y}_i}{\partial \bar{y}} = 0, i = o, f \end{cases} \end{aligned} \quad (11-a)$$

$$\begin{aligned} \bar{x} = 0, -\bar{\ell}_{sy} < \bar{y} < 0 \text{ or } \bar{x} = \bar{\ell}_x, -\bar{\ell}_{sy} < \bar{y} < 0 \\ \text{or } \bar{y} = -\bar{\ell}_{sy}, 0 < \bar{x} < \bar{\ell}_x \frac{\partial \bar{T}}{\partial \bar{l}} = 0 \end{aligned} \quad (11-b)$$

Initial conditions;

$$\bar{T} = 0, \bar{Y}_f = 0 \text{ and } \bar{Y}_o = 1. \quad (12)$$

Here $\bar{w}_g = \bar{Y}_o \bar{Y}_f \bar{A}_g \exp\left(-\frac{\bar{E}_g}{\bar{T} + \bar{T}_\infty}\right)$,

$$\bar{w}_c = \bar{A}_c \exp\left(-\frac{\bar{E}_c}{\bar{T} + \bar{T}_\infty}\right),$$

$$\bar{m} = K_e \int_{-\bar{\ell}_{sy}}^0 \bar{\rho}_c \bar{w}_c d\bar{y}, \text{ and}$$

$$\bar{T}_\infty = C_{ps} T_\infty / L_s.$$

The dimensionless groups are listed in Table 1.

Numerical Approach

The computational domain of approximately 15 mm × 15 mm, in the streamwise (x) direction and transverse (y) direction consists of a 50 × 50 mesh system in the gas phase and a 50 × 40 mesh system in the condensed material. Along the x direction the grid spacing is uniformly 0.3 mm. Along the y direction the grid spacing is

TABLE 1

Dimensionless Parameters for the Numerical Model			
Symbol	Parameter group	Symbol	Parameter group
\bar{A}_g	$\frac{A_g \rho_g \alpha_s Y_{0\infty}}{u_\infty^2}$	\bar{A}_c	$\frac{A_c \alpha_s}{u_\infty^2}$
\bar{q}_g	$\frac{q_g Y_{0\infty} C_{Ps}}{\mu_o C_{Pg} L_s}$	\bar{q}_c	$\frac{q_c C_{Ps}}{C_{Ps} L_s}$
\bar{E}_g	$\frac{E_g C_{Ps}}{R L_s}$	\bar{E}_c	$\frac{E_c C_{Ps}}{R L_s}$
Le	$\frac{\alpha_g}{D}$	St	$\frac{C_{Ps}(T_m - T_\infty)}{L_s}$
\bar{C}_{Pl}	$\frac{C_{Pl}}{C_{Ps}}$	$\bar{\rho}_l$	$\frac{\rho_l}{\rho_s}$
$\bar{\rho}_c$	$\frac{\rho_c}{\rho_g}$	\bar{k}_l	$\frac{k_l}{k_s}$
\bar{v}_{n^*}	$\frac{v_{n^*}}{u_\infty}$	$\bar{\ell}_{sy}$	$\frac{u_\infty \ell_{sy}}{\alpha_s}$
\bar{q}_{ig}	$\frac{\dot{q}_{ig} \alpha_s C_{Ps}}{u_\infty k_s L_s}$	$\bar{\omega}$	$\frac{\epsilon \sigma \alpha_s L_s^3}{k_s u_\infty C_{Ps}^3}$

non-uniform with the minimum spacing (0.025 mm) near the gas-condensed interface ($y = 0$) with an exponential increase in the two opposite (y_{0+} and y_{0-}) directions. The neighboring increment ratio is 1.07. This treatment is intended to resolve the reaction-intensive region close to the interface. The mappings between the two mesh systems were accomplished by appropriate coordinate transformations.

The finite difference method is used to solve the numerical model [17]. First, the control volume formulation is used in the discretization because of its ability for providing exact tracking of the solid-liquid interface during phase change in the condensed material. The diffusion terms are treated by the central difference method; the convective term by the up-wind scheme, which in low flow velocity provides acceptable performance. To treat the chemical (source) terms, the guideline of positive derivatives of source terms is followed. Negative chemical terms are linearized by preserving only the partial derivatives with respect to the primary variable, whereas the positive source term is left unchanged. In addition, a special treatment of the chemical term is used to enhance the accuracy and stability of the solution procedure [18]. To minimize computational time and storage, the ADI (Alternate Direction Implicit)

method is employed: the independent variables are solved alternately in the x and y directions. The techniques used in solution of the phase change process in the condensed phase is a special form of the Enthalpy Method, the ADI Source Update Method, as well as the aforementioned enthalpy-temperature relationship. In addition, property discontinuities across the solid-liquid interface are averaged by using the harmonic mean formulation [19] of the thermal properties for any grid encompassing this interface.

The run time is influenced by three major nonlinearities that are present in the numerical model. These nonlinearities are the interface condition, the chemical reaction terms in the gas and condensed material, and the Stefan condition. It was determined by numerical experiments that the stiffness of the overall equations, hence the run time, is determined mainly by the chemical reactions. This overshadows the influence of phase change even at high Stefan numbers. In views of the nonlinear nature of the numerical model, the iterative Newton-Raphson scheme is applied in semi-implicit form to the finite difference equation.

The computational cycles are constructed according to the physical process. First the energy equation of the condensed phase is solved, which produces the gas-condensed interface pyrolysis product flow rate and the interface temperature. Next this flow rate is fed into the boundary conditions of the two species equations, and the gas-condensed interface temperature is fed into the boundary condition of the energy equation in the gas. After the gas phase temperature is solved from the energy equation, the heat flux of the interface is obtained as a further input into the condensed phase. The iterative computational process continues until the relative error of the two most recent iterative values of T , Y_o , Y_f , and h_c fall into the convergence range, the limit of which is normally chosen as 0.0001.

Theoretical (Simple) Model

The model configuration for theoretical analysis is shown in Fig. 3. The coordinate system is flame-fixed, hence a streamwise convection term is introduced in the energy equation of the

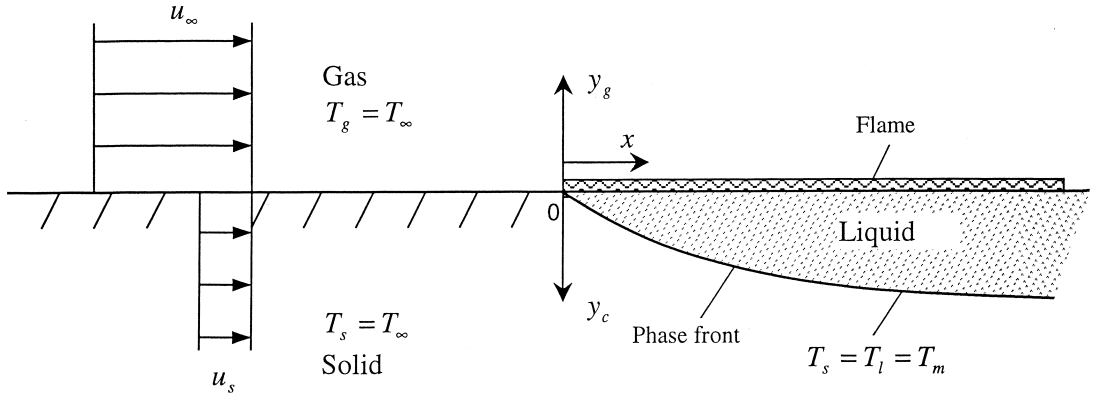


Fig. 3. The simplified flame-spread model for steady spread of an opposed-flow diffusion flame over a semi-infinite condensed phase.

condensed phase. The global energy balance principle of Wichman and Williams [6] is applied. The global energy balance principle states that the “flame spread rate must be sufficient to remove by downstream solid-phase convection (in flame fixed coordinates) the heat that is generated by combustion and not removed by either downstream gas-phase convection or conduction.” This global balance principle is valid when either solid or gas phase conduction overpowers the other, whereas a simplified energy balance for heat flow to unignited fuel across surfaces of incipient fuel [2] can be used only when gas-phase conduction overpowers solid-phase conduction. Thus, flame spread models that employ an energy balance across the flame leading edge (and in its vicinity) are not so generally applicable as the global energy balance. With gas-phase domination both leading edge and global balance models should give approximately identical predictions. For most leading-edge models it has been demonstrated [3, 6, 7] that under most conditions encountered in flame spread, gas-phase domination is the norm. Exceptions to this norm are discussed in Ref. [20], where the viscous-inviscid region near the point of flame attachment is examined in detail. The authors of [20] demonstrated that an upstream gas-phase fluid dynamic recirculation cell could alter flame spread behavior.

In applying the energy balance principle, the Oseen approximation is employed. The flame sheet is hypothesized to lie along the gas-condensed material interface. The transition from solid material to liquid is assumed to occur

across an infinitesimally thin front located at the locus of a parabolic arc $y/\sqrt{x} = const$. All of the latent heat is presumed to be consumed along this arc. In addition, the liquid is presumed to be sufficiently viscous that internal, circulating flows do not occur as they do for certain light, hydrocarbon liquids. The analytical solution yields the following spread rate formula (see Appendix A),

$$\frac{u_f}{u_\infty} = \frac{\rho_g C_{pg} k_g}{\rho_l C_{pl} k_l} \cdot \left(\frac{T_f - T_i}{T_i - T_m} \right)^2 \cdot \operatorname{erf} \left(c \sqrt{\frac{1}{2} \cdot \frac{\alpha_s}{\alpha_l}} \right)^2, \quad (13)$$

where T_f is the flame temperature, T_i is the interface temperature (see Fig. 3), and c is the value of the numerical constant defining the locus of the liquid-solid interface. As $c \rightarrow 0$ and $T_m \rightarrow T_i$, Eq. 13 reduces to the thick fuel deRis formula [5].

When phase change occurs, the Stefan number $St = C_{ps}(T_m - T_\infty)/L_s$ appears as one of the nondimensional parameters of the problem. Physically, St is the ratio of the heat required to raise a unit mass of the solid from the ambient temperature to its melting temperature to the heat required to transform this unit mass of solid into liquid. Only $St > 0$ is of interest to us because St is positive when phase change is endothermic. A derivation of the preceding results is presented in the Appendix.

²In this model, the definition of St is inverse to those appearing in [3] and [8].

Simplified Derivation of Flame-Spread Equation

In this section, a simple, physically motivated-scaling-argument derivation is given for Eq. 13. A full description is presented in the Appendix. The simplicity of the scaling analysis sheds light on the important approximations of the analysis. It was shown in [3, 6, 7] that for a basic understanding of the overall flame spread process only the energy conservation equations of both media were needed, and that in these equations a balance between streamwise convection and traverse diffusion (a boundary-layer formulation) captured most of the physics. The full problem is elliptic, as shown in numerous original works [5, 21], but the region of pure ellipticity is confined to a small “Stokes region” near the flame attachment point. Outside of that small region, a parabolic formulation produces useful results. We follow the scaling analysis outlined in [3, 20].

We proceed by first scaling the three energy equations (gas, liquid melt, and solid), then the boundary conditions along the interfaces (gas-liquid, liquid-solid) that separate them. In the gas energy equation $\rho_g C_{Pg} u_g \partial T_g / \partial x = k_g \partial^2 T_g / \partial y^2$ scales to $\rho_g C_{Pg} u_g \Delta T_g / L_{gx} \sim k_g \Delta T_g / L_{gy}^2$. Imposition of the criterion $L_{gx} = L_{gy} = L_g$, i.e., uniform coordinate scaling in the flame attachment region gives $L_g = \alpha_g / u_g$, $\alpha_g = k_g / \rho_g C_{Pg}$. In the solid the energy equation is $\rho_s C_{Ps} u_s \partial T_s / \partial x = k_s \partial^2 T_s / \partial y^2$, which scales to $\rho_s C_{Ps} u_s \Delta T_s / L_{sx} \sim k_s \Delta T_s / L_{sy}^2$. We let $L_{sx} = L_{gy} = L_g$ to emphasize gas-phase control of the spread process. We then find $L_{sy} = [\alpha_s \alpha_g / u_s u_g]^{1/2}$. Similarly, the liquid-phase energy equation $\rho_l C_{Pl} u_l \partial T_l / \partial x = k_l \partial^2 T_l / \partial y^2$ scales to $\rho_l C_{Pl} u_l \Delta T_l / L_{lx} \sim k_l \Delta T_l / L_{ly}^2$, which yields $L_{ly} = [\alpha_l \alpha_g / u_l u_g]^{1/2}$ when we use $L_{lx} = L_{gx} = L_g$ as for the solid. Clearly $u_l = u_s$.

We now examine the two interfaces. Along the solid-gas interface upstream of the flame attachment point, the conductive energy balance gives $k_s (\partial T_s / \partial y)_{y=0} \sim k_g (\partial T_g / \partial y)_{y=0}$, which yields $k_s \Delta T_s / L_{sy} \sim k_g \Delta T_g / L_{gy}$ or $L_{sy} / L_g = k_s \Delta T_s / (k_g \Delta T_g)$. Along the liquid-solid interface, the situation is more complicated. Here we have $k_s (\partial T_s / \partial n^*) \sim k_l (\partial T_l / \partial n^*)$, where n^* is the normal coordinate to the parabolic arc along which phase change occurs. This

arc is given by the locus $y = -b_l x^2$, which nondimensionalizes to $\bar{y} = -\bar{x}^2$ with $\bar{y} = y / L_{ly}$, and $\bar{x} = x / L_{lx} = x / L_g$ and $L_{ly} = b_l L_g^2$. In the case that the parabolic arcs lie nearly parallel to the horizontal plane, the derivatives $\partial T / \partial n$ approximate to $\partial T / \partial y$. Thus, the nondimensionalization of the interface condition yields, approximately, $k_s \Delta T_s / L_{sy} \sim k_l \Delta T_l / L_{ly}$. Use of $L_{ly} = b_l L_g^2$ gives

$$k_s \frac{\Delta T_s}{L_{sy}} \sim \frac{k_l}{b_l L_g} \frac{\Delta T_l}{L_g}. \quad (14)$$

In our derivation this interface condition is considered to be more important to the overall spread process than the solid-gas interface condition derived previously. Hence we substitute the relationship $L_{sy} = [\alpha_s \alpha_g / u_s u_g]^{1/2}$ derived from the solid-phase energy equation into Eq. 14 to obtain

$$u_s = u_g \frac{\alpha_s k_l^2}{\alpha_g k_s^2} \left(\frac{\Delta T_l}{\Delta T_s} \right)^2 \frac{1}{b_l L_g} \quad (15)$$

The expression for $\Delta T_l / \Delta T_s$ is now written in the following form: $\Delta T_l / \Delta T_s = (\Delta T_g / \Delta T_l) (\Delta T_l / \Delta T_s)^2 (\Delta T_s / \Delta T_g)$. Then we use Eq. 14 for $\Delta T_l / \Delta T_s$ in the right-hand side (square) term, and the upstream interface condition $k_s \Delta T_s / L_{sy} = k_g \Delta T_g / L_{gy}$ for $\Delta T_s / \Delta T_g$. These expressions substituted into Eq. 15 yield

$$\frac{u_s}{u_g} = \frac{\rho_g C_{Pg} k_g}{\rho_l C_{Pl} k_l} \left(\frac{\Delta T_g}{\Delta T_l} \right)^2 \left[\frac{\alpha_s}{\alpha_l} (b_l L_g)^2 \frac{L_g^2}{L_{sy}^2} \right].$$

The quantity in square brackets reduces to $(\alpha_s / \alpha_l) (L_{ly} / L_{sy})^2$ when the relationship $L_{ly} = b_l L_g^2$ is employed. When we observe that both liquid and solid must produce parabolic isotherms, we find $(L_{ly} / L_{sy})^2 = (b_l / b_s)^2 = \kappa^2$, where $L_{sy} = b_s L_g^2$ was used in the solid. The constant factor κ is nondimensional. Thus, our final result is

$$\frac{u_s}{u_g} = \frac{\rho_g C_{Pg} k_g}{\rho_l C_{Pl} k_l} \left(\frac{\Delta T_g}{\Delta T_l} \right)^2 \left[\kappa^2 \frac{\alpha_s}{\alpha_l} \right] \quad (16)$$

We compare this result to Eq. 13, the exact formula, by considering the limit of small c (high sweep-back of the isotherms) to find $\text{erf}[c\sqrt{\alpha_s/2\alpha_l}] \approx (2\sqrt{\pi})[c\sqrt{\alpha_s/2\alpha_l}]$. This yields Eq. 16 with the quantity in square brackets replaced by $(2c^2/\pi)\alpha_s/\alpha_l$. The correspon-

TABLE 2

Major Properties and Kinetic Data Used for the Numerical Model

$k_s = 0.05 \text{ W}/(\text{m} \cdot \text{K})$	$C_{ps} = 1460 \text{ J}/(\text{kg} \cdot \text{K})$	$\rho_s = 1190 \text{ kg}/\text{m}^3$	$\rho_l = 1190 \text{ kg}/\text{m}^3$
$T_m = 500 \text{ K}$	$A_c = 2.82 \times 10^9 \text{ s}^{-1}$	$E_c = 129580 \text{ J}/\text{mol}$	$q_c = 1113.5 \text{ kJ}/\text{kg}$
$K_c = 0.5$	$k_g = 0.0411 \text{ W}/(\text{m} \cdot \text{K})$	$C_{pg} = 1007 \text{ J}/(\text{kg} \cdot \text{K})$	$\rho_g = 1.16 \text{ kg}/\text{m}^3$
$D = 3.514 \times 10^{-5} \text{ m}^2/\text{s}$	$A_g = 1.6 \times 10^{15} \text{ m}^3/(\text{kg} \cdot \text{s})$	$E_g = 155000 \text{ J}/\text{mol}$	$q_g = -15539.4 \text{ kJ}/\text{kg}$
$u_\infty = 0.1 \text{ m}/\text{s}$	$T_\infty = 300 \text{ K}$	$Y_{O_\infty} = 0.31$	$Y_{f_\infty} = 0.0$

dence between the two formulas is exact when we identify $\kappa^2 = 2c^2/\pi$. We note finally that in Eq. 16 $\Delta T_g = T_f - T_s$, $\Delta T_l = T_s - T_m$ are the characteristic temperature difference in the gas and liquid phases, respectively.

This simplified analysis illustrates important features of the phase change model of flame spread. First, the gas phase is elliptic near the flame leading edge because $L_{gx} = L_{gy} = L_g$, i.e., all characteristic lengths in the 2-D plane are identical. Second, in the limit being considered chemistry is very fast compared with convection and diffusion processes. Third, the solid and liquid phases are fundamentally parabolic, with streamwise diffusion $\partial^2(\cdot)/\partial x^2$ negligible in comparison with transverse diffusion $\partial^2(\cdot)/\partial y^2$. Fourth, conduction across the interfaces between gas and solid (upstream) and liquid and solid (downstream) dominates streamwise convection and the phase change enthalpy, which appears only implicitly in the parameter c of Eq. 13. Fifth, of the two interfaces, the energy balance across the solid-liquid interface was used more than the solid-gas interface balance, indicating its greater importance in the overall flame spread process. Sixth, simple rearrangement of Eq. 16 gives $u_s = \kappa^2 u_g [(\rho_g C_{Pg} k_g)/(\rho_s C_{Ps} k_l)] \bar{k}_l^{-1} (\Delta T_g/\Delta T_l)^2$, suggesting that u_s decreases in proportion to \bar{k}_l^{-1} and in proportion to C_{ps}^{-1} , if their influences on other parameters are not considered. Our subsequent evaluations demonstrate that $u_s \propto \bar{k}_l^{-1}$ is a good reckoning, whereas $u_s C_{ps} \sim \text{constant}$ is not (see Figs. 4(B) and (C)). Seventh, the concept of “gas-phase dominance” of the spread process is implicitly understood by the imposition of the gas-phase length L_g on L_{lx} and L_{sx} ; i.e., the use of $L_{lx} = L_{sx} = L_g$. Eighth, the liquid layer is highly viscous so that no internal convection or recirculation occurs. Although surface tension gradients produced by temperature gradients along the interface can induce circulatory liquid

movement [22], we have not included these motions in our scaling analysis. Ninth, subject to the constraint of Oseen flow (which can be removed as discussed in [7]) and fast chemistry, the largest influences on the flame spread rate are the thermal properties of gas, solid and liquid, and the Stefan number, whose magnitude controls the multiplicative factor κ^2 in (16) (c in Eq. 13).

RESULTS AND DISCUSSION

The thermal and flow properties are listed in Table 2. Ignition is established if the heat flux from the gas phase excluding external radiation is over $10 \text{ W}/\text{cm}^2$. The effects of the condensed material on flame spread are investigated by varying three nondimensional parameters, St , \bar{k}_l , and \bar{C}_{Pl} , in which St denotes the influence of phase change, and \bar{k}_l and \bar{C}_{Pl} denote the relative influence of liquid thermal properties. Variation of St , \bar{k}_l , and \bar{C}_{Pl} is accomplished by changing only one single property L_s , k_l , or C_{Pl} whereas keeping the rest fixed.

Flame Spread Rate

The thick fuel spread rate of deRis’s formula [5] is

$$\frac{u_s}{u_\infty} = \frac{\rho_g C_{Pg} k_g}{\rho_s C_{Ps} k_s} \left(\frac{T_f - T_v}{T_v - T_\infty} \right)^2, \quad (17)$$

where T_v denotes the vaporization temperature.³ Because T_f and T_v are theoretical parameters that correspond approximately to real

³The vaporization temperature T_v in deRis’s formula is essentially equivalent with the surface temperature T_i in Equation (13) as the latter denotes the constant temperature of the non-vaporizing surface although the former denotes solid-to-gas “vaporization” (actually sublimation).

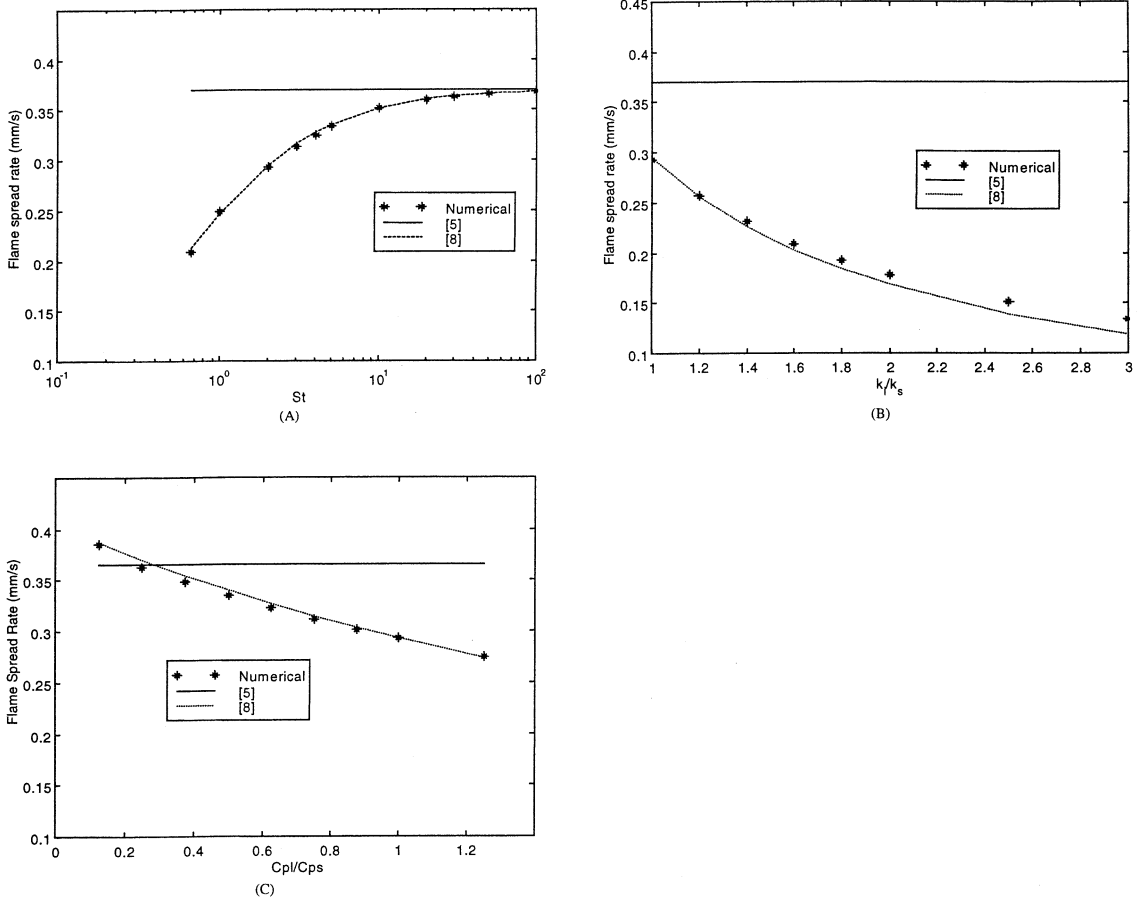


Fig. 4. (A) Flame spread rate vs. St ; (B) Flame spread rate vs. \bar{k}_l at $St = 2$; (C) Flame spread rate vs. \bar{C}_{pl} at $St = 2$.

condensed-phase and combustion kinetics, and because they are in fact not constant in the numerical model, representative values have to be selected in order to make a comparison. Based on the numerical results of the interfacial temperature (see Fig. 8-A) and on previous experimental measurement ($T_v = 665$ K for PMMA), it is a reasonable guess to fix T_v at 700 K. We extract T_f from Eq. 13 by letting the u_s equal the numerical flame spread at $St \rightarrow \infty$, because $St \rightarrow \infty$ corresponds exactly to flame spread without phase change, that is, the flame spread problem is essentially characterized by deRis's formulation. It is worth pointing out that this treatment helps to make a comparison between Eq. 13 and the numerical model. This comparison is justifiable in that no artificial manipulation is involved for situations of widely varying thermal properties. Therefore, we obtained the following representative values, $T_f =$

1730 K, thus resulting in the following ratio of the right hand side of Eq. 14

$$\left(\frac{T_f - T_v}{T_v - T_\infty} \right) = 2.58.$$

We note that this ratio remained fixed in all cases considered, and that $T_f = 1730$ K is a physically reasonable flame temperature estimated in flame spread since the maximal flame temperature in the numerical results is 1630 K. In effect, a scaling factor has been introduced that makes the case $St \rightarrow \infty$ agrees with the deRis formula. The dependence of the flame spread rate on St , which is obtained from Eqs. 13, 17, and the numerical model, is plotted separately in Figs. 4-A through -C. Figure 4-A reports the dependence of flame spread on St by presenting the formulas of and eleven computational results. It seems that the formula

provides an almost an exact solution to the spread rate of the numerical model, since agreement between the numerical results (“*”) and theory (dotted curve) is observed. However, Eq. 17, which is represented by a horizontal solid line above the “*” and dotted lines, results in a constant value higher than both the numerical result and theory. Qualitatively, with the increase of St , the spread rate increases. The sensitivity of the spread rate with respect to St , which is illustrated by the slope of the curve in Fig. 4-A, diminishes for larger St . In addition, St is inversely proportional to L_s , and an almost linear relationship between spread rate and L_s is found. As a result, the aforementioned sensitivity with respect to L_s is almost constant.

We can estimate the influence of phase change on the spread rate. The contribution of phase change can be as much as a 40% change of the flame spread formula at $St = 1$ and nearly negligible influence at $St = 100$. Through numerical experiments, it was found that if St is lower than 0.667, only ignition is observed, followed by extinction. No flame spread occurs. Since the external heat flux is removed as soon as ignition is initiated in the numerical model (for all St cases), the above finding indicates that the flame cannot support itself if St is too low.

The contributions of \bar{k}_l and \bar{C}_{pl} to the flame spread rate for $St = 2$ are reported in Figs. 4-B and 4-C, respectively. Good agreement is observed. Qualitatively, the increase of either the conductivity or the thermal capacity of the liquid layer in the condensed phase decreases the flame spread rate. Similarly, extinction is observed if \bar{k}_l is lower than approximately 1.0, or \bar{C}_{pl} is higher than approximately 1.25. Again, Eq. 13 does not provide any indication of extinction because of the steady state formulation. However, one may conjecture that certain limits can be derived from the three cases of varying St , \bar{k}_l , and \bar{C}_{pl} . Therefore, extinction occurs if the ideal (Eq. 13) spread rate decreases below these limits. These rate limits are dependent on parametric values. This viewpoint is partly supported by observing that the rate limits of Fig. 4-A, -B, and -C differ from each other significantly. However, it is difficult to determine these rate limits quantitatively because extinction is not a well-defined event in the numerical

model.⁴ One reason is that the control of grid size or convergence procedure may influence and substantially alter such unstable phenomena. It may be necessary, therefore, to examine flame extinction at least partly analytically. Even in analytical studies, however, the precise definition of the moment of ignition is an ill-defined quantity.

Transient Spread Process

Figure 5-A reports the progress of flame spread rate along the streamwise distance for $St = 2$. Three stages of transient evolution are observed, viz., ignition, transition and fully developed (or steady) spread. Ignition is characterized by sharp slopes of flame spread rate around a peak point, indicating the impulsive nature of the ignition process. The transition stage, which occurs after ignition, allows the flame to stabilize mainly over the preheated region (9–12 mm). Its behavior is characterized by smaller slopes. The final stage of the spread is established after the flame moves across the boundary between the pristine polymer and preheated region ($x = 9$ mm), and the flame spreads with constant rate. Figure 5-B reports the time histories of both flame front and phase front arrival along the polymer surface. It is observed that the interval of transition (2 s), compared to the ignition delay time (10 s), is relatively short. Another observation is that the movement of the phase front started much earlier than the flame front. This phenomenon arises from the fact that the phase front is established much earlier than the flame front, because the melting temperature is much lower than the ignition temperature. In Fig. 5-B, the phase front leads the flame in the region $9 \text{ mm} < x < 10 \text{ mm}$. The streamwise progress of the phase front is the described as follows: shortly after the initial heating the phase front starts to move, then it approaches the boundary of the preheating region, shown in Fig. 5-A at the location between $x = 9$ and $x = 12$ mm. Between this time and ignition, the phase front can not move because there is no heat flux applied outside the

⁴A very detailed analysis of flame spread initiation was carried out in Ref. 9, where all gas-phase processes including thermal expansion were retained.

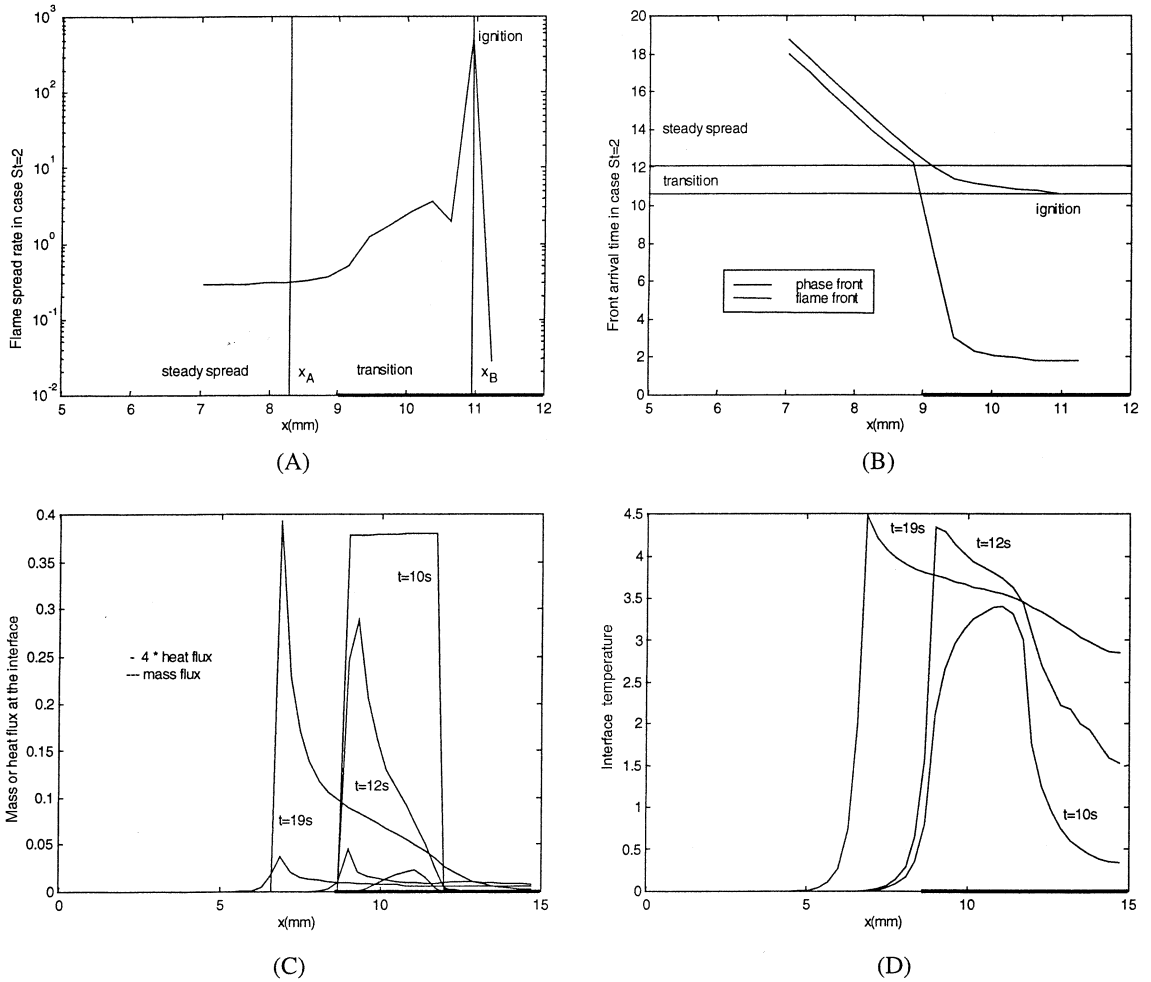


Fig. 5. (A) Flame spread rate vs. streamwise distance at $St = 2$ (the front propagates to the left); (B) Arrival times of flame front and phase front vs. streamwise distance; (C) The streamwise evolution of heat and mass flux at the interface before ignition (10s), during transition (12s) and during steady spread (19s); (D) The streamwise evolution of interface temperature before ignition (10s), during transition (12s) and during steady spread (19s).

preheating region. Even with ignition initiated, the flame front still stays put because the external heat flux is removed and the self-supportive heat flux is too weak to push it forward. The resumption of movement is not accomplished until the flame survives the transition and spread near the boundary of the preheating region. Thereafter, phase spread is driven by the combustion heat from the gas phase and steady spread is attained. This steady stage is characterized by the same spread rate as for the phase front, as is seen by the two parallel lines in Fig. 5-B.

Figures 5-C and -D report the streamwise

evolution of heat flux,⁵ mass flux, and temperature at the interface during three stages of flame spread. At the time of pre-ignition (10 s), an external heat flux of 5 W/cm^2 is applied to the preheating region of the surface; the mass flux of pyrolysis products is low because of the low condensed phase temperature, see Fig. 5-D. Once ignition is initiated, the external heat flux

⁵The heat flux here denotes the net heat flux feeding the condensed phase, which is obtained by subtracting the surface radiation loss from gas phase conduction to the interface.

is removed, and an abrupt change of flame environment occurs. The plume of the flame adapts to the rapid change of the heat flux, during which transition occurs. If, for example, the heat flux generated from the combustion reaction cannot compete with the loss of heat through the gas and the condensed phase, the plume shrinks and extinction takes place, as was observed earlier in the article. The transition stage determines whether the flame is self-supportive or not. Figures 5-C and -D illustrate the successful survival of the plume and steady spread thereafter. It is observed in Fig. 5-C that the magnitude of the heat flux during the steady spread stage is approximately one tenth of the external heat flux. However, the mass flux shows a reverse trend with an increase of magnitude by a factor of ten because the low mass flux of the initial stage results from the thin pyrolysis layer. Steady spread is attained when the mass flux attains the highest value and heat flux attains the lowest value among the three stages.

As far as the interface temperature is concerned, a leading edge appears after ignition, whose magnitude slightly increases to attain the steady state. Downstream of the leading edge during the steady spread stage, the surface temperature decreases with increase of distance from the leading edge. This observation disagrees with the assumption of a constant surface vaporization temperature discussed at length in [3]. The invalidity of the assumption was discussed in numerical studies (that did not consider the effects of phase change) such as [13, 14]. The divergence of the temperature downstream of flame front from an assumed constant value at the leading edge is as high as 20% for the case $St = 2$. Apparently such a deviation is not crucial, given the eventual agreement between numerical results and theory. For this reason, the constant "vaporization temperature" hypothesis has survived and, in fact, represents an important conceptual piece of the overall flame spread model.

Flame Structure

The detailed flame structure is obtained from the numerical model by examining contours of constant temperature, fuel concentration, oxidizer concentration, and combustion reaction

rate in four cases of interest (see Fig. 6). The non-dimensional temperature from the numerical model is divided by St to make comparisons. From the viewpoint of physics, the flame structure displayed in Fig. 6 shows qualitatively the same characteristic as reviewed in [3]. Under the influence of an opposed flow, the diffused fuel gas from the interface (Fig. 6-C) reacts with the oxidizer gas in the mainstream (Fig. 6-D), thereby forming a reaction region (Fig. 6-B). From Fig. 6-B we see that the thickness of the reactive region is finite, which shows the nature of finite-rate reaction in the gas. In addition, the temperature of this reactive region is the highest in the field, as shown in Fig. 6-A. The highest temperatures are displaced from the surface somewhat downstream of the reactivity maximum, as observed in previous studies of flame near cold surfaces [23–25].

It is interesting to evaluate the influence of the condensed phase on the flame structure. A reference state of $St = 2$ is chosen for these comparisons. First, it is observed from Fig. 6-A that $St = 100$ and $\bar{k}_l = 3$ produce bigger flames. However, $\bar{C}_{pl} = 0.125$ produces a smaller flame. This observation is confirmed by comparing fuel concentration constant contours in Fig. 6-C. The same constant contour of fuel concentration is pushed further downstream of the flame leading edge if $St = 100$ or $k_l = 3$. The second observation is from Fig. 6-B. Near the flame leading edge, the shape and orientation of the reactive region does not change for the four cases we examined; however, farther downstream of the flame leading edge, the reactive region tends to be slightly raised if St or \bar{k}_l becomes larger, or slightly pressed down if \bar{C}_{pl} becomes smaller.

The Condensed Phase

The temperature profile (including location of the phase front) from both the numerical model and theory are compared in Fig. 7. Theory predicts that the isotherms are parabolas with the origins located at the leading edge 'o' in Fig. 7. The numerical solution, however, predicts that the isotherms do not resemble the shape of parabola except near the flame leading edge. The isotherms deviate from parabolas downstream of the leading edge. The thickness of the

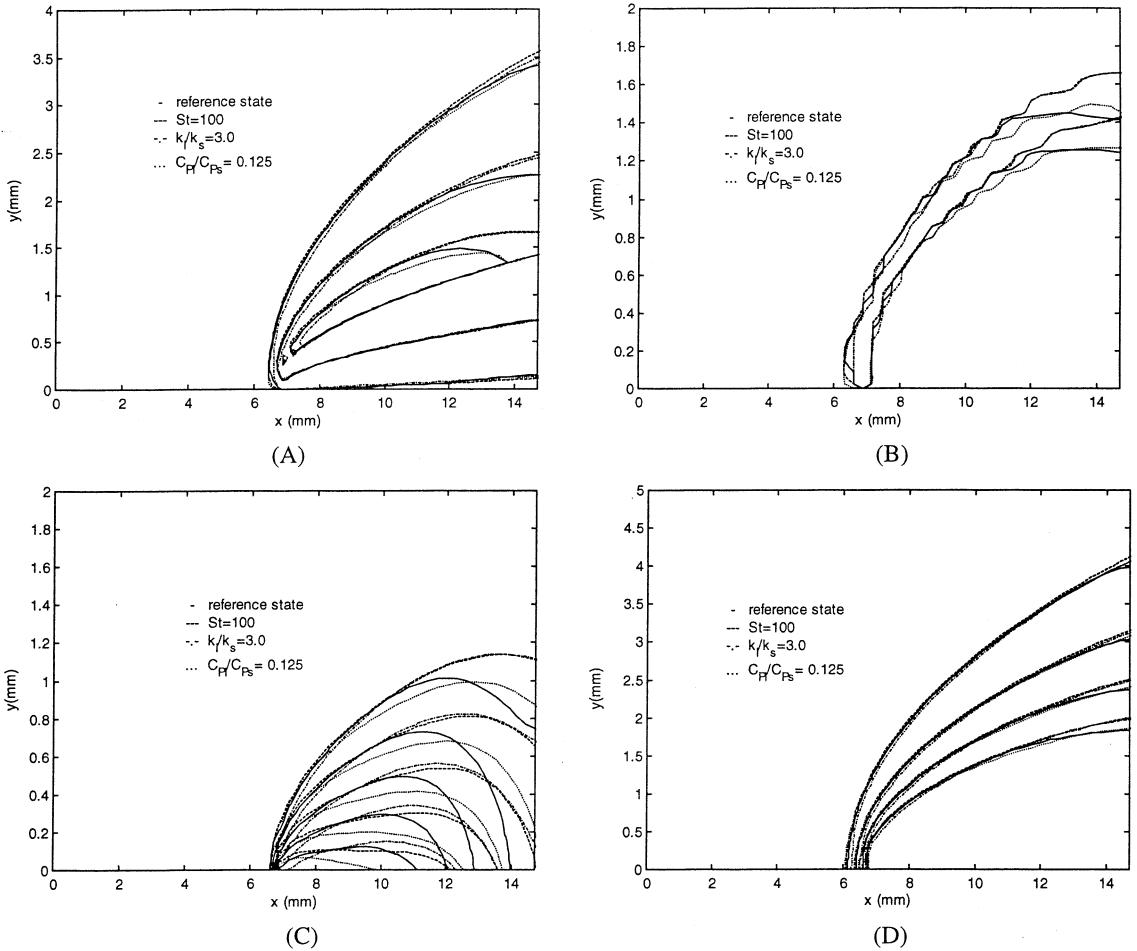


Fig. 6. Comparisons of non-dimensional (A) temperature/ St , (B) reaction rate, (C) fuel concentration and (D) oxidizer concentration for four conditions of the condensed material. The outermost isotherm is 2.0 with increment 2.0 between two adjoining contours; the innermost isoline of oxidizer or fuel is 0.2 with increment 0.2 between two adjoining contours; the reaction profile is characterized by reaction rate 0.0001.

liquid layer shrinks downstream. Good agreement between the numerical result and theory is observed near the leading edge of the phase change point 'o.' The behavior of the liquid thickness downstream of the leading edge suggests a connection to the surface temperature or heat flux at ignition, therefore some other parameters of interest are investigated.

The influence of the condensed phase on flame spread during the steady spread stage is shown in Fig. 8 by investigation of interface temperature, mass flux, condensed phase heat conduction and the phase front locations. As is shown by the interface temperature in Fig. 8-A, there is negligible difference downstream of the

flame front among four cases except $\bar{k}_l = 3$. In addition, upstream of the flame front, $St = 100$ produces a shallower gradient of the interface temperature than $St = 2$, and $C_{Pl} = 0.125$ makes this gradient even lower. Distributions of the interface mass flux and the net heat flux into the condensed phase along the streamwise distance are presented in Figures 8-C and 8-D. Among the four cases, $\bar{k}_l = 3$ stands out having the highest mass flux and lowest heat conduction into the condensed phase. This phenomenon is well understood if we recall that we used the in-depth pyrolysis mechanism in the condensed phase. As a result, the larger pyrolysis area in general corresponds to a higher mass

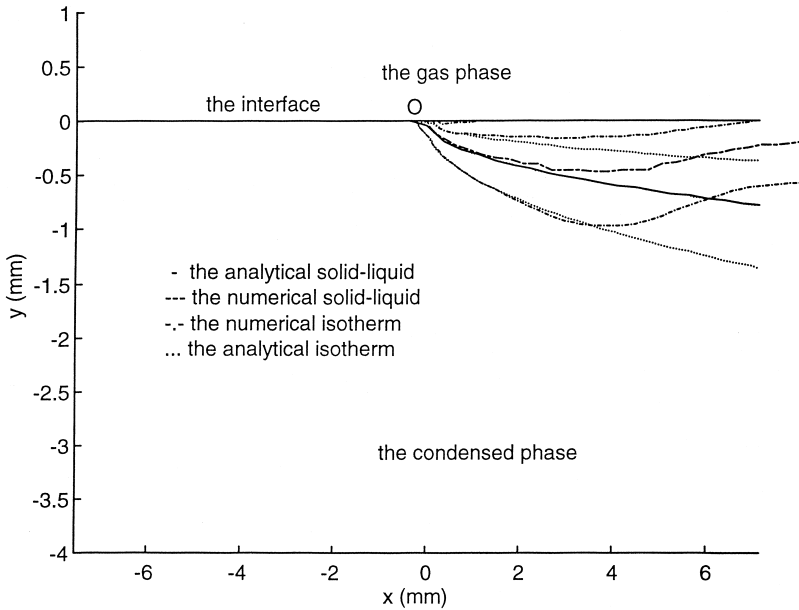


Fig. 7. Comparison of numerical model and theory (Appendix) for the temperature profiles and phase fronts in the condensed phase at $St = 2$. The location of phase change coincides with the constant profile $\bar{T} = St$. The lowest isotherm is 1.0 with increment 1.0 between two adjoining contours. The analytical isotherm of $\bar{T} = 4$ coincides with the straight line of the gas-condensed interface.

flow rate. The extent of the pyrolysis area is related to the extent of the melting region, as shown in Fig. 8-B. It is observed that $\bar{k}_l = 3$ significantly enlarges the liquid region, thus resulting a higher pyrolysis region, whereas in the other cases a smaller difference is observed.

A simple analysis illustrates that \bar{k}_l controls the thickness of the liquid phase. The liquid layer in the condensed phase can be looked on as a plane plate, the upper side of which is subjected to the ignition temperature T_{ig} , and the lower side of which is subjected to the melting temperature T_m . If \bar{q}_{ig} denotes the heat conduction into the condensed phase, then a simple heat conduction relation applies if the transient effect is neglected,

$$\delta = k_l \frac{T_{ig} - T_m}{\bar{q}_{ig}}, \tag{18}$$

where δ denotes the average thickness of the liquid layer. Because the magnitudes of \bar{q}_{ig} and T_{ig} do not depend significantly on the magnitude of \bar{k}_l , an approximate relationship of $\delta \propto k_l$ is determined. This explains why the liquid layer thickness of $\bar{k}_l = 3$ is almost three times as large as $\bar{k}_l = 1$.

The streamwise evolution of the phase front location and pyrolysis front location (characterized by $\bar{w}_c = 1.5 \times 10^{-7}$) is shown in Fig. 9. The liquid region encompasses almost the entire pyrolysis region during all three stages. In addition, the slight intrusion of the pyrolysis front out of the phase boundary indicates that the pyrolysis temperature is slightly lower than the melting temperature. Also the shape of the pyrolysis region is not a parabola. Its thickness shrinks downstream of the flame front and fits well with the shape of phase front. In addition, the reaction intensive part of the pyrolysis region has the highest temperature, and lies below the flame front.

Mechanism of Steady Flame Spread

Generally, many different mechanisms contribute to the flame spread process, and conclusions on which mechanism is dominant (if any) are difficult to make. The dependence of flame spread on St , \bar{k}_l , and \bar{C}_{Pl} is analyzed below. Control volumes of $5.7 \text{ mm} \times 4.5 \text{ mm}$ upstream of the flame leading edge are chosen for cases $St = 100$, $\bar{k}_l = 3$, $\bar{C}_{Pl} = 0.125$ as well as the

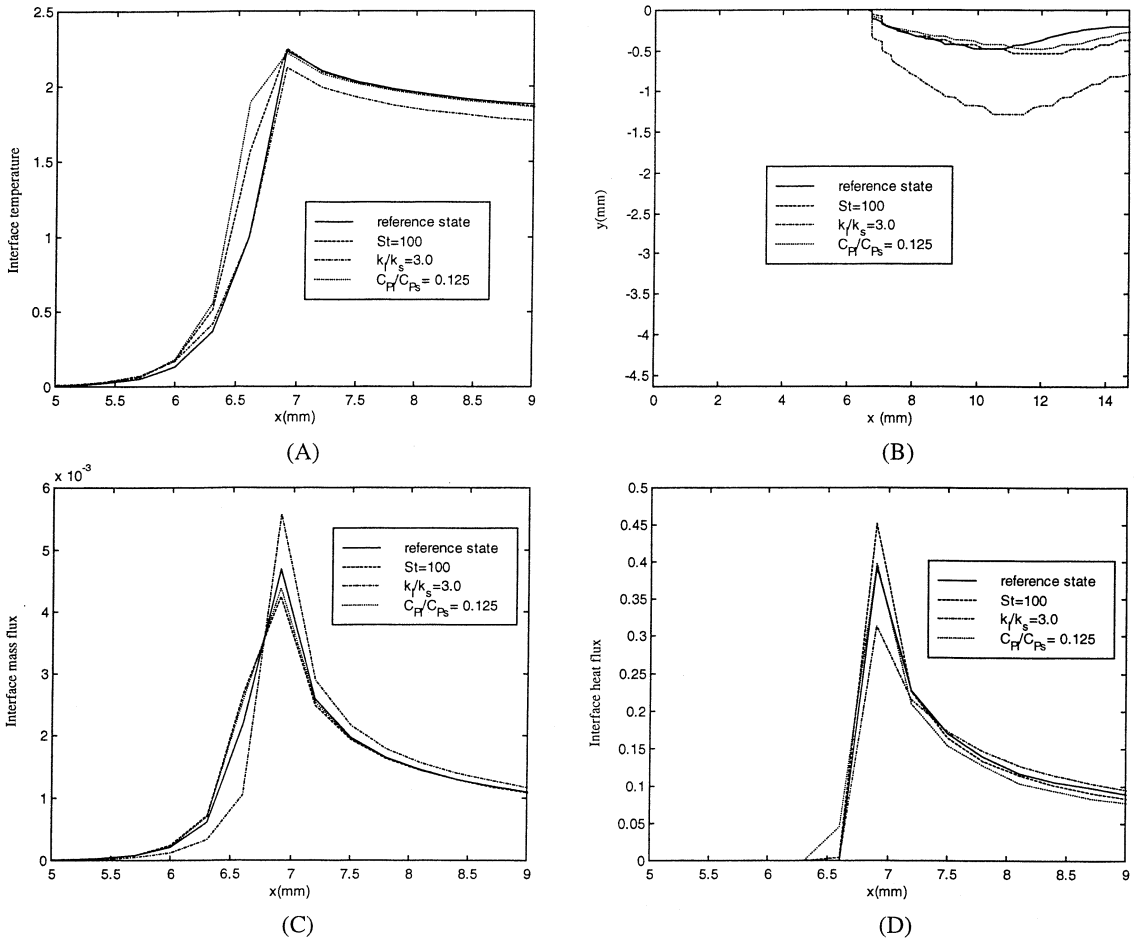


Fig. 8. Comparisons of (A) interface temperature, (B) phase location, (C) interface mass flux and (D) interface heat flux in four situations of the condensed phase.

reference state to construct a local energy-balance accounting. Different heat transfer mechanisms in nondimensional form are evaluated by numerical integration, see Table 3.

An energy balance can be constructed for this control volume. The heat from the gas phase upstream of the flame leading edge plus the streamwise conduction in the condensed phase are responsible for the pyrolysis process and enthalpy rise of the control volume. Pyrolysis and streamwise conduction in the condensed phase are not important compared with the upstream conduction from the gas phase [2]. Physically, the total heat obtained in Table 3 is responsible for enthalpy rise of the control volume, and should be connected to the spread rate. Comparison of $St = 2$ and $St = 100$ in Table 3 indicates that with the increase of St ,

the total heat increases, resulting in a higher spread rate. However, for cases of variable thermal conductivity and variable heat capacity, the magnitudes of the total heat do not necessarily measure the magnitudes of the spread rate. This phenomenon can be explained by a ratio between the total heat and the spread rate.

The ratio of the total heat to the spread rate, presented in Table 3, denotes the energy barrier for flame propagation with a spread rate of unity. We compare this ratio for the four cases we examined, since it reflects physically the ratio of relative difficulty of preheating the condensed phase to the ignition temperature. This ignition temperature (the temperature at the flame leading edge), should be identical for different cases if justifiable deductions are made. Observation of Fig. 8-A indicates that

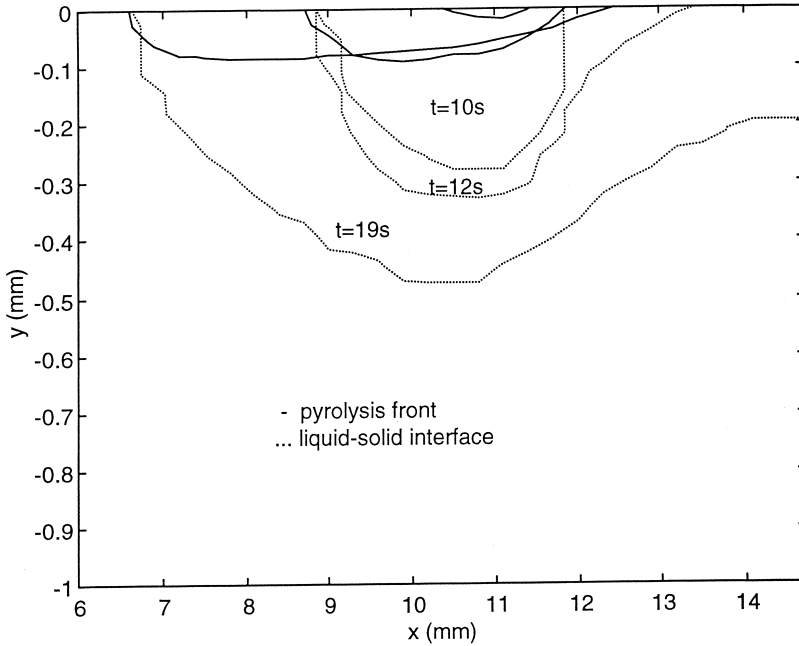


Fig. 9. The evolution of solid-liquid interface and pyrolysis front locations before ignition (10s), during transition (12s) and during steady spread (19s). The pyrolysis front is characterized by $\bar{w}_c = 1.5 \times 10^{-7}$ in the numerical model.

$St = 2$, $St = 100$, $\bar{C}_{Pl} = 0.125$ have identical flame temperatures at the leading edge, therefore comparisons between these three cases are made below. From Table 3 the ratio for $St = 100$ has a lower value than for $St = 2$, indicating a lower energy barrier when the latent heat is decreased. Similarly, the ratio for $\bar{C}_{Pl} = 0.125$ is lower than for the reference state, because the lower thermal capacity is consistent with the lower energy barrier. A different interpretation for the last case $\bar{k}_l = 3$ is needed because it shows many different characteristics from the other cases. From Fig. 8-A, it is

observed that $\bar{k}_l = 3$ results in a lower flame temperature at the leading edge. Second, from Fig. 8-B, $\bar{k}_l = 3$ results in a larger liquid thickness. The first influence tends to lower the ratio in Table 3 because a lower ignition temperature is required. The second influence, however, tends to increase the ratio because a thicker liquid layer requires more energy. The overall influence of $\bar{k}_l = 3$ seems to be controlled by the second influence, as is supported by Table 3: the ratio of the total heat to the spread rate is larger than for the reference state.

TABLE 3

Different Heat Transfer Mechanisms in Four Cases of Interest, in which $St = 2$ Serves as the Reference State

	$St = 2$	$St = 100$	$\bar{k}_l = 3$	$\bar{C}_{Pl} = 0.125$
(Heat conduction from gas phase—radiation at the interface)	2.497	2.828	1.406	2.231
Streamwise conduction in the condensed phase	3.229	4.279	11.042	1.965
Heat of pyrolysis in the condensed phase	0.0000	0.0000	0.0000	0.0000
The total heat	5.727	7.107	12.448	4.196
Spread rate (10^{-4} m/s)	2.926	3.677	1.316	3.852
The total heat/Spread rate	1.957	1.932	9.458	1.089

CONCLUSIONS

A new numerical model of flame spread is constructed by introducing phase change in the condensed phase. The processes considered in the condensed phase include solid-to-liquid phase change, an in-depth pyrolysis reaction and heat conduction. The processes in the gas phase, after applying the Oseen-flow approximation, include heat transfer, fuel and oxidizer transfer, and finite-rate combustion kinetics. At the interface between the gas phase and the condensed phase, the heat and mass balance is constructed by incorporating heat conduction into both gas and condensed phases, radiant emission from the surface, and diffusion of pyrolysis products into the gas.

The influence of phase change and thermal properties of the condensed phase on flame spread are investigated by introducing three non-dimensional parameters of interest, St , \bar{k}_l , and \bar{C}_{pl} . Quantitative comparisons of spread rate between the numerical model and theory outlined in previous sections, and Appendix are obtained. It is found that the numerical model provides almost exact correspondence to [8] for variable St and \bar{C}_{pl} , and 90% agreement for cases of variable \bar{k}_l . deRis's flame spread formula, which results in a constant spread rate value higher than the numerical result and Eq. 13, is independent of phase change.

Some observations are made about the transient process of flame spread. (1) Three stages are observed: ignition, transition, and fully developed (or steady state) flame spread. In addition, the interval of transition is found to be very short compared to the ignition delay time. (2) Extinction is observed if St , \bar{k}_l go below, or \bar{C}_{pl} goes beyond, certain limits. Quantitative values of these limits are not precisely known. (3) The rates of spread of the phase and flame fronts differ until the steady spread stage is attained.

The dependence of flame structure on St , \bar{k}_l , and \bar{C}_{pl} were studied. With the increase of St or \bar{k}_l , or with the decrease of \bar{C}_{pl} , the flame size increased. These results are consistent with the qualitative nature of the dependence of the flame spread rate on the three parameters. Physically, a lower latent heat or a lower thermal capacity means a lower energy barrier for the flame, hence a larger spread rate. The

increase of \bar{k}_l , on the other hand, denoting the diffusion away of the thermal energy for preheating, results in a lower spread rate. The study of heat flux, mass flux and surface temperature at the interface provides additional information on the mechanisms of flame spread.

The mechanisms of flame spread are interpreted by energy balance analysis. It is found that a ratio between the total heat applied to the condensed material upstream of the flame leading edge and the spread rate reveals the physical mechanisms that control the preheating of the condensed material to the ignition temperature. A comparison on this basis is consistent with the notion of a "fundamental equation of flame spread" as discussed originally in [2] and in Section 3.1.5 of [3]. This equation is written as $q = \rho_s u_f \Delta h$, where q is the energy flux transported across the flame front to upstream unburned fuel, ρ_s is the fuel density, and Δh is the fuel thermal enthalpy difference between ignition and ambient temperature. Clearly, the quantity $q/u_f = \rho_s \Delta h$ was evaluated in our work, and this quantity has the direct physical relevance to the propensity for flame spread. Comparisons of this ratio in situations of varying St , \bar{k}_l , and \bar{C}_{pl} reveals the difference in physical mechanisms that control the preheating of the condensed phase to the ignition temperature. Although the theoretical result (Eq. 13) on which much of the numerical comparisons were based and where predictions were, in some cases, remarkably accurate when compared with numerical results, it was derived from the application of the global energy balance principle [6]. The general result it produces (Eq. 13) can subsequently be examined in terms of *local* energy balances. Thus, there is no contradiction between a globally derived formula and its subsequent local interpretation.

Extension of the current work is needed. The transient flame behaviors, such as extinction limit or ignition limit with phase change, leave room for future research. In addition, detailed analysis of the mechanisms of flame spread over a melting polymer is needed. More attention may be given to combination of the gas phase influence with phase change processes in the condensed material. Further modeling efforts may be attempted by incorporating the melt

flow phenomena when the burning material is no longer horizontal.

The support of the National Institute of Standards and Technology (NIST) (Building and Fire Research Division) through contract number 71NANB9D0091, monitored by Dr. Kathryn M. Butler, is gratefully acknowledged.

APPENDIX

The flame-spread formula of Eq. 13 is derived mathematically. This model examined here is built upon that of [8]. The spread mechanism is driven by a “surface flame” located along the gas-condensed phase interface [6]. Following [8] we assume negligible upstream conduction in both gas and solid, thereby invoking the global energy balance principle described at length therein (see [6]). The energy equation in the three phases are given by $\rho_j u_j C_{Pj} \partial T_j / \partial x = k_j \partial^2 T_j / \partial y^2$ where $j = g, l, s$ and $u_l = u_s$. For the gas we have $0 < x < \infty, y > 0$, for the liquid $0 < x < \infty, 0 < y < f(x)$, for the solid $0 < x < \infty, y > f(x)$, where $y = f(x)$ describes the shape of solid/liquid interface. Along this contour, we are able to write the interfacial energy balance in the form $k_{l1}[(\partial T_l / \partial x)^2 + (\partial T_l / \partial y)^2]^{1/2} = k_s[(\partial T_s / \partial x)^2 + (\partial T_s / \partial y)^2]^{1/2} + \rho_s u_s L_s \{(\partial f / \partial x) / [(\partial f / \partial x)^2 + (\partial f / \partial y)^2]^{1/2}\}$, where L_s is the enthalpy of liquefaction (positive) and the third term in the energy balance represents the liquefaction energy flux along the liquefaction front $y = f(x)$. We define dimensionless variables $\tau_j = (T_j - T_\infty) / (T_i - T_\infty), j = g, l, s, \xi = x / L, \eta = y / L$ ($L = \lambda_s / \rho_s C_{Ps} u_s$) where T_i is the downstream gas-liquid interface temperature (gasification or “vaporization” temperature). The equations, when transformed into parabolic cylinder coordinates $\xi = (s^2 - n^2) / 2, \eta = sn$ ($n = \text{constant}$ defines a family of parabolic arcs with $n = 0$ the downstream gas/liquid interface $y = 0, x > 0$). The governing equations transform to $N_j n d\tau_j / dn = -d^2 \tau_j / dn^2, j = g, l, s$ with $N_g = [u_g / u_s][\alpha_s / \alpha_g], N_l = (\alpha_s / \alpha_l), N_s = 1$. Along the liquid/solid interface we have $\tau_l = \tau_s = \tau_m$ and $\Lambda[\tau_{l,\xi}^2 + \tau_{l,\eta}^2]^{1/2} = [\tau_{s,\xi}^2 + \tau_{s,\eta}^2]^{1/2} + \tau_m St \hbar \xi / [\hbar_\xi^2 + \hbar_\eta^2]^{1/2}$, where $\Lambda = \lambda_l / \lambda_s, St = L_s / C_{Ps} (T_m - T_\infty)$ and \hbar is non-dimensional h . Along this interface we have $n =$

$c = \text{constant}$. In terms of (s, n) the interface condition above simplifies to the form $\Lambda \tau_{l,n} = \tau_{s,n} + \tau_m St c$. The remaining conditions are $\tau_g = \tau_l = 1$ at $n = 0, \tau_l = \tau_s = \tau_m$ at $n = c, \tau_g$ and τ_s vanish as $n \rightarrow \infty$ in each medium.

The energy equations are easily solved in terms of error functions. The liquid/solid interface condition yields the following parametric relationship:

$$\Lambda \frac{(1 - \tau_m)}{\tau_m} \sqrt{N_l} \frac{\exp\left(-\frac{N_l c^2}{2}\right)}{\text{erf}\left(c \sqrt{\frac{N_l}{2}}\right)} + \frac{\exp\left(-\frac{c^2}{2}\right)}{\text{erfc}\left(\frac{c}{\sqrt{2}}\right)} = c \sqrt{\frac{\pi}{2}} St \tag{A.1}$$

We note that as $T_m \rightarrow T_i$ and $c \rightarrow 0$ the preceding equation gives $\text{erf}(c \sqrt{N_l} / 2) / (T_i - T_m) \rightarrow \Lambda \sqrt{N_l} / (T_i - T_m) = [\rho_l C_{Pl} \lambda_l / \rho_s C_{Ps} \lambda_s]^{1/2} / (T_i - T_\infty)$, which further reduces to the flame spread formula of [5]. Equation 13 for the spread rate is derived using the method of Ref. 8. We write the net heat flux from the surface flame (at $y = 0, x > 0$) as $q_f = -\lambda_g \partial T_g / \partial y - \lambda_l \partial T_l / \partial y = [\sqrt{u_g} \rho_g C_{Pg} \lambda_g + \sqrt{u_s} \rho_l C_{Pl} \lambda_l \sqrt{\Phi}] [T_i - T_\infty] / \sqrt{\pi x}$, where $\Phi = \Lambda^2 N_l$. When we also write $q_f = (T_f - T_\infty) \sqrt{\rho_g C_{Pg} \lambda_g} / \sqrt{\pi x}$ we obtain the flame-spread formula

$$\frac{u_f}{u_\infty} = \frac{\rho_g C_{Pg} k_g}{\rho_l C_{Pl} k_l} \cdot \left(\frac{T_f - T_i}{T_i - T_m}\right)^2 \cdot \text{erf}\left(c \sqrt{\frac{1}{2} \cdot \frac{\alpha_s}{\alpha_l}}\right)^2$$

which is Eq. 13. We note that $St > 0$ is for ordinary endothermic solid \rightarrow liquid liquefaction. As noted in [8], the first term in Eq. A.1 is the nondimensional heat flux to the interface from the liquid and it becomes infinite as $c \rightarrow 0$, zero as $c \rightarrow \infty$. The second term is the nondimensional heat flux leaving the interface into the solid, and it approaches unity as $c \rightarrow 0$ and infinity linearly with c as $c \rightarrow \infty$ (since $\lim_{x \rightarrow \infty} \text{erfc}(x) = \sqrt{\pi} x \exp(x^2)$). The third term is the heat absorbed at the solid/liquid interface.

REFERENCES

1. Fernandez-Pello, A. C., Hirano, T., *Combust. Sci. Technol.* 32:1-31 (1983).
2. Williams, F. A., *Sixteenth Symposium (International) on*

- Combustion*, The Combustion Institute, Pittsburgh, 1976, p. 935–948.
3. Wichman, I. S., *Prog. Energy Combust. Sci.* 18:553–593 (1992).
 4. Ross, H. D., *Prog. Energy Combust. Sci.* 20:17–63 (1994).
 5. deRis, J. N., Ph.D. thesis, Harvard University, 1968.
 6. Wichman, I. S., and Williams, F. A., *Combust. Sci. Technol.* 32:91–123 (1983).
 7. Wichman, I. S., *Combust. Flame* 50:287–304 (1983).
 8. Atreya, A., *Eighth International Heat Transfer Conference*, San Francisco (1986).
 9. MacGrattan, K. B., Kashiwagi, T., Baum, H. R., and Olson, S. L., *Combust. Flame* 106:377–391 (1996).
 10. Kashiwagi, T., *Twenty-fifth Symposium (International) on Combustion*, The Combustion Institute, Irvine 1994, p. 1423–1437.
 11. Fernandez-Pello, A., and Williams, F. A., *Combust. Flame* 28:251–277 (1977).
 12. Frey, A. E., and Tien, J. S., *Combust. Flame* 36:263–189 (1979).
 13. Di Blasi, C., and Continillo, G., *The Use of Computers in Chemical Engineering, Proceedings of Chemical Engineering Fundamentals XVII Congress*, Giardini-Nixos, 1987, p. 261.
 14. Bhattacharjee, S., and Altenkirch, R. A., *Combust. Flame* 84:160–169 (1991).
 15. Nayagam, V., and Williams, F. A., *Physical Rev. Lett.* 84(3):479–482 (2000).
 16. Hostler, S. R., and Nayagam, V., *Proceedings of Central States Sections of the Combustion Institute*, 218–223, Indianapolis (2000).
 17. Patankar, S. V., *Numerical Heat Transfer and Fluid Flow*, McGraw-Hill, NY (1980).
 18. Shih, T. I-P., and Chyu, W. J., *ALAA J.* 29:1759–1760 (1991).
 19. Voller, V. R., *Advances in Numerical Heat Transfer*, Vol. 1, Taylor & Francis (1997).
 20. Higuera, F. J., Linan, A., and Iglesias, Z., *Combust. Theory and Model.* 1:65–78 (1997).
 21. Sirignano, W. A., *Acta Astronautica* 1:1285–1299 (1974).
 22. Sirignano, W. A., and Glassman, I., *Combust. Sci. Technol.* 1:307–312 (1970).
 23. Wichman, I. S., Lakkaraju, N., and Ramadan, B., *Combust. Sci. Technol.* 127:141–165 (1997).
 24. Wichman, I. S., and Ramadan, B., *Physics of Fluids* 10(12):3145–3154 (1998).
 25. Chen, C. H., and Tien, J. S., *Combust. Sci. Technol.* 50:283–306 (1986).

Received 13 September 1999; revised 20 June 2000; accepted 31 August 2000